



# Influence of the catalyst layer thickness on the determination of the OER activity of $\text{Fe}_3\text{O}_4@\text{CoFe}_2\text{O}_4$ core-shell nanoparticles

Lisa Royer<sup>a</sup>, Julie Guehl<sup>a</sup>, Maud Zilbermann<sup>a</sup>, Thierry Dintzer<sup>a</sup>, Cédric Leuvrey<sup>b</sup>, Benoit P. Pichon<sup>b,c</sup>, Elena Savinova<sup>a</sup>, Antoine Bonnefont<sup>d,e,\*</sup>

<sup>a</sup> UMR 7515 CNRS-ECPPM-Université de Strasbourg, ICPEES, 25, rue Becquerel, Cedex 2, Strasbourg F 67087, France

<sup>b</sup> Université de Strasbourg, CNRS, Institut de Physique et Chimie des Matériaux de Strasbourg, UMR 7504, Strasbourg F-67000, France

<sup>c</sup> Institut Universitaire de France, 1 rue Descartes, Cedex 05, Paris 75231, France

<sup>d</sup> Institut de Chimie, UMR 7177, CNRS-Université de Strasbourg, 4 rue Blaise Pascal, CS 90032, cedex, Strasbourg 67081, France

<sup>e</sup> University Grenoble Alpes, University Savoie Mont Blanc CNRS, Grenoble INP (Institute of Engineering, University Grenoble Alpes), LEPMI, Grenoble 38000, France

## ARTICLE INFO

### Keywords:

Impedance spectroscopy  
Transmission line model  
Porous electrode  
Nanoparticles  
Oxygen evolution reaction

## ABSTRACT

Transition metal oxides-based catalytic layers often present a complex 3D porous architecture affecting the evaluation of their intrinsic electrocatalytic activity. In this work the oxygen evolution reaction activity of core-shell  $\text{Fe}_3\text{O}_4@\text{CoFe}_2\text{O}_4$  nanoparticles combining a conductive magnetite core and a catalytically active cobalt ferrite shell was studied at different loading and thickness of the catalytic layer. It was observed that their apparent activity is decreasing and that the Tafel slopes are becoming convex when the loading increases. The activity decay could be attributed to the significant resistance to charge transport in the thick porous catalyst layer. This resistance could be estimated by fitting the electrochemical impedance spectra using the transmission line model. The influence of the layer thickness on the experimental current-potential curves and on their Tafel slopes could be simulated using a simple model based on the Telegrapher's equations. It is concluded that in order to measure accurately the activity and Tafel slopes of an electrocatalyst, thin layers must be used, notably for catalyst layers that are not highly conductive.

## 1. Introduction

Anion exchange membrane water electrolysis is an attractive alternative to proton exchange membrane water counterpart allowing the replacement of the iridium anodes by more abundant 3d transition metal oxides (TMO) based on nickel, cobalt, iron or manganese [1,2]. TMOs with spinel structure constitute a promising class of oxygen evolution reaction (OER) catalysts due to their high electrocatalytic activity, a relatively low synthesis temperature allowing the preparation of high surface area catalysts and their composition-dependent and widely tunable properties [3,4].

Benchmarking of TMOs is usually performed in aqueous electrolytes by depositing a catalyst layer on the surface of an inert substrate enclosed in a rotating disk electrode (RDE) setup. However, the TMO-based catalytic layers often present a complex 3D porous architecture affecting the evaluation of their intrinsic activity. Indeed, the packing of the catalyst particles (here nanoparticles (NPs)) within the structure determines the porosity of the assembly, i.e. the active surface area of

NPs, as well as the charge transport between them, i.e. the conductivity of the layer. In the case of the OER in an aqueous alkaline electrolyte, the performance of the catalyst layer can be affected by: the water  $/\text{OH}^-$  transport in the catalyst layer which depends on the porosity of the layer; the efficiency of the  $\text{O}_2$  removal and eventually the formation of  $\text{O}_2$  bubbles that might block the access to catalytic active sites; local changes of the pH affecting the stability and the activity of the layer; electronic conduction across the layer which depends on the intrinsic conductivity of the catalyst materials composing the layer and/or on the contact resistance between the catalyst particles.

At room temperature, the electronic conductivity of TMOs is usually not very high. Thus, to compensate for this lack of conductivity, carbon is often added to the catalytic layers for benchmarking of TMOs. Numerous TMO-based catalysts for the OER have been studied in the literature and these materials generally presented a low conductivity if no carbon was added to the catalytic layer [1,2] However, carbon materials are oxidized at high anodic potentials required for the OER [5]. Hence, carbon addition could be eventually used to determine the

\* Corresponding author.

E-mail address: [pierre-antoine.bonnefont@grenoble-inp.fr](mailto:pierre-antoine.bonnefont@grenoble-inp.fr) (A. Bonnefont).



activity of TMOs but it won't be possible to use it at the anode of a water electrolyzer on an industrial scale. Another possibility is to develop electrocatalysts based on TMOs with high intrinsic electronic conductivity such as  $\text{Fe}_3\text{O}_4$ , that is conductive thanks to an electron hopping between the Fe (II) and Fe (III) cations [6]. However, even if  $\text{Fe}_3\text{O}_4$  nanoparticles possess high intrinsic conductivity, the conductivity of NP networks may be low due to the contact resistance between the NPs, the conductivity mainly involving the tunneling of electrons between the NPs [7,8]. Thus, to accurately evaluate electrocatalytic activity of such materials it is critically important to consider charge transport through the catalytic layer and understand whether the entire surface of the catalytic material is involved in the electrochemical reaction.

In order to understand better the effect of the catalyst conductivity, Chung et al. [9] reported on how the electrical resistance of the catalytic layer affects its hydrogen evolution electrocatalytic activity. They investigated poorly conductive amorphous and crystalline  $\text{MoS}_2$  (loading  $0.25 \text{ mg.cm}^{-2}$ ) mixed with various amounts of carbon and demonstrated that both the overpotential and the Tafel slope are affected by underutilization of the active material and the ohmic losses in the catalyst layer. Indeed, increase of the ohmic resistance resulted in an increase of the overpotential (required to reach a  $10 \text{ mA.cm}^{-2}$  current density per geometric surface) from 0.15 to 0.35 V and Tafel slope from 40 to  $75 \text{ mV.dec}^{-1}$ . Additionally, for poorly conductive catalysts they observed an inflexion in the Tafel plots that deviated from a linear behavior and became convex. They concluded that while electrical conductivity of the catalyst layer is often neglected in electrocatalytic studies, it should be considered as one of the important criteria when designing electrocatalysts.

In the past years, electrochemical impedance spectroscopy (EIS) has been successfully applied to the study of porous electrodes. [10–13]. In many cases, the impedance spectra obtained on porous electrodes could be reasonably fitted by using distributed-element models such as the transmission line model. For example, Papaderakis et al. [14] studied the OER on porous iridium oxide catalytic layers in acidic solution and used the transmission line model to evaluate the charge transfer resistance and capacitance for different loadings. By studying the impedance spectra at potentials below and in the potential range of the OER, they concluded that impedance studies of porous  $\text{IrO}_2$  electrodes can give an estimate of their total capacitance  $C_t$  and that this capacitance decreases during the OER due to the pore clogging by evolved  $\text{O}_2$ .

We report here on OER active nanoparticles which combine a magnetite core and a cobalt ferrite shell:  $\text{Fe}_3\text{O}_4@\text{CoFe}_2\text{O}_4$ . These well-defined NPs with a narrow size distribution and controlled shape and composition both for the core and the core-shell were synthesized via a seed-mediated growth based on the thermal decomposition of metal complexes as recently reported [15,16]. Such a core-shell structure allows combining an electrochemically active phase (Co-Ferrite) at the nanoparticle surface and a conductive  $\text{Fe}_3\text{O}_4$  core. [7,8] Even though the shell is not conductive, this conductive core is expected to enhance the electron transport between the current collector and the interface between the nanoparticles and the electrolyte. They also present the advantage of using low amounts of cobalt, an element which demand is exploding worldwide and which has been classified as critical material by the European union recently [17]. In what follows, the influence of the thickness of  $\text{Fe}_3\text{O}_4@\text{CoFe}_2\text{O}_4$  catalyst layer on the determination of the intrinsic OER activity is discussed for two catalyst samples with different NPs diameters, 9 nm and 14 nm by using voltammetry, Tafel slope analysis and electrochemical impedance spectroscopy.

## 2. Materials and methods

The core-shell  $\text{Fe}_3\text{O}_4@\text{CoFe}_2\text{O}_4$  NPs were obtained via a seed-mediated growth based on the thermal decomposition of iron (II) and cobalt (II) stearate complexes. These metal complexes were synthesized following already published procedures for the iron stearate [18] and the cobalt stearate [15]. In a 1 L two-necked round-bottom flask, 9.8 g

(32 mmol) of sodium stearate (98.8%) were poured and 320 mL of distilled water were added. The mixture was heated to reflux under magnetic stirring until all the stearate was dissolved. Afterward, 3.80 g (16 mmol) of iron (II) chloride tetrahydrate (or 3.16 g (16 mmol) of cobalt (II) chloride hexahydrate) dissolved in 160 mL of distilled water was poured in the round-bottom flask. The mixture was heated to reflux and kept at this temperature for 15 min under magnetic stirring before cooling down to room temperature. The colored precipitate was collected by centrifugation (15 000 rpm, 5 min) and washed by filtration with a Buchner funnel. Finally, the powder was dried in an oven at  $65^\circ\text{C}$  for 15 h.

### 2.1. Core-shell 9 nm NPs

Core shell  $\text{Fe}_3\text{O}_4@\text{CoFe}_2\text{O}_4$  NPs having an average diameter of 9 nm (denoted CS-9 in the following) were prepared using the following procedure [15,16]. The core (iron oxide NPs) was synthesized using an already published protocol [3]. A two-necked round-bottom flask was filled with 1.38 g (2.22 mmol) of iron (II) stearate, 1.254 g (4.44 mmol) of oleic acid (99% Alfa Aesar) and 20 mL of dioctyl ether (BP =  $290^\circ\text{C}$ , 97% Fluka). The brownish mixture was heated at  $100^\circ\text{C}$  under a magnetic stirring for 30 min in order to remove water residues and to homogenize the solution. The magnetic stirrer was then removed and the flask was connected to a reflux condenser before heating the solution to reflux for 2 h with a heating ramp of  $5^\circ\text{C/min}$ . At the end, the mixture was allowed to cool to  $100^\circ\text{C}$ . 4 mL of the solution was taken to characterize the NPs core. After cooling at room temperature, this 4 mL fraction was precipitated by the addition of acetone and washed by agitation with a magnetic stirrer in warm acetone ( $60^\circ$ ). They were then stored in chloroform.

The other fraction was used to perform a second thermal decomposition and synthesize the shell by adapting an already published protocol [16]. After a cooling down step 0.335 g (0.531 mmol) of cobalt stearate (II) was dissolved in 20 mL of octadecene and subsequently added to the remaining solution. The reaction medium was heated again at  $100^\circ\text{C}$  for 30 min under magnetic stirring to remove water residues and to homogenize the solution. After removal of the magnetic stirrer, the flask was connected to a reflux condenser to heat the solution at reflux for 3 h under air with a heating rate of  $1^\circ\text{C/min}$ . Finally, after cooling to room temperature, the nanoparticles were precipitated by the addition of acetone to wash them by agitation with a magnetic stirrer in warm acetone ( $60^\circ\text{C}$ ) for 1 h. They were then stored in chloroform.

### 2.2. Core-shell 14 nm NPs

The iron oxide core of the NPs was synthesized using iron stearate (III), the synthesis protocol was developed by F. Pertion [19]. 2 g (2.2 mmol) of commercial iron (III) stearate, 1.23 g of oleic acid (99% Alfa Aesar), 19.5 mL of squalene and 0.5 mL of dibenzyl ether were used for the core synthesis. After the homogenization step, the flask was connected to a reflux condenser before heating the solution to reflux for 1 h with a heating ramp of  $5^\circ\text{C/min}$ . After cooling, the NPs were precipitated, washed and stored in chloroform.

For the shell synthesis half of the already washed core NPs was taken and the chloroform was evaporated with a rotavapor. 0.456 g (0.73 mmol) of cobalt (II) stearate, 0.914 g (1.47 mmol) of iron (II) stearate, 1.27 g of oleic acid, 10 mL of dioctyl ether, and 20 mL of 1-octadecene were added to the reaction medium. After the homogenization step, the flask was connected to a reflux condenser and kept at reflux for another 2 h with a heating ramp of  $1^\circ\text{C/min}$ . After cooling, the NPs were precipitated and washed.

### 2.3. Electrochemical measurements

The NPs were drop-casted on a clean and polished glassy carbon (GC) electrode ( $d = 0.5 \text{ cm}$ ) and a 3-electrode cell was used with a 0.1 M



NaOH electrolyte to characterize the material electrochemically. The working electrode (WE) was a glassy carbon on top of which the NPs have been drop-casted, the counter electrode (CE) was a gold wire, and the reference electrode (RE) was a Hg/HgO/0.1 M NaOH whose potential was regularly measured vs. RHE to make sure that it was stable in time.

First, 50 cycles of cyclic voltammetry (CV) were done between 0.83 and 1.43 V vs. RHE with a scan rate of  $100 \text{ mV s}^{-1}$  in order to clean the surface and to get rid of the oleic acid/ organic molecules that can surround the NPs. After that, some slower rate ( $10 \text{ mV s}^{-1}$ ) cyclic voltammetry measurements were performed and the Tafel slopes plots were constructed from the IR corrected positive scans of the CV by dividing the current by the catalyst mass. Upon observation that for high loadings the Tafel slopes were deviating from the ideal linear behavior, the Tafel slopes were determined by fitting the linear parts of the Tafel plots around two different potentials:  $1.62 \pm 0.15$  and  $1.67 \pm 0.15$  V vs. RHE. The impedance measurements were performed at 1.62 V vs. RHE. The range of frequency was from 0.2 to 10 kHz with 10 points per decade. The electrolyte resistance was determined from the high frequency part of the impedance spectra (100 Hz). The catalyst loading on the GC electrode varied from 131 to  $1.3 \mu\text{g.cm}^{-2}$  for CS-9 and 42.8 to  $0.7 \mu\text{g.cm}^{-2}$  for CS-14. Measurements were performed on a Gamry potentiostat REF 600. All experiments were repeated at least three times to confirm their reproducibility. The electrochemical results will only be exploited for a current density lower than  $1 \text{ mA.cm}^{-2}$  to avoid the influence of the  $\text{O}_2$  bubble formation and the mass transport issues.

#### 2.4. SEM characterization

NPs were drop-casted onto either a silicon wafer or a GC plate (1 mm thick) at different loadings in order to analyze their spatial arrangement on the substrate. Cross-sections were obtained by breaking the substrates and then subjecting them to an argon ion beam using IM4000plus cross polisher at 6 keV voltage. Silicon substrates were submitted to the beam for 45 min. Thus, obtained cross sections were characterized by scanning electron microscopy (SEM) with a Zeiss Gemini SEM 500 scanning electron microscope with a lattice resolution of 1 nm using SE-Inlens (secondary electrons) detector at 1 keV voltage,  $15.00 \mu\text{m}$  aperture and the working distance 3 mm. Before taking the images, the samples were cleaned with  $\text{N}_2$  plasma generated by an evactron (power 20 W for 2 min). Since the quality of the cross-sectional images was much higher when using the flat silicon wafer substrate, they will be used for further analysis.

#### 2.5. TEM micrographs

The TEM images were obtained on a JEOL 2100 LaB6 instrument with a 0.2 nm point-to-point resolution. Transmission electron microscopy (TEM) data were used to calculate the mean size of NPs with a standard deviation, in measuring the size of 200 NPs with the Image J software. High-resolution image of the NPs were taken to clarify whether NPs comprise of single crystals. The chemical composition of the NPs was investigated with energy dispersive spectroscopy (EDS). The Fast Fourier Transformation and the microscopy images treatment and analysis were done using the Digital Micrograph software.

#### 2.6. XRD measurements

Measurements were performed on a Bruker D8 Advance diffractometer equipped with a non-monochromatic copper radiation ( $K\alpha = 0.154,056 \text{ nm}$ ) and a Sol-X detector in the  $20-80^\circ 2\theta$  range with a  $0.02^\circ$  step. High-purity silicon powder (lattice parameter  $a = 0.357,082 \text{ nm}$ ) was systematically used as an internal standard.

### 3. Results and discussion

#### 3.1. Characterization of the NPs and NP layers

In this work, two types of NPs were used: CS-9 and CS-14. Their characterization showed that the NPs are homogeneous in size, shape, and composition. Their size, structure and crystallinity have been confirmed by X-ray diffraction (Fig. 1A), transmission electron microscopy (Fig. 1B, C, E, F) and the core-shell structure has been confirmed thanks to the electron energy loss spectroscopy (EELS) mapping [20]. They display an average diameter of 9.3 nm and 14.0 nm respectively (Fig. 1D) and are presenting X-ray diffraction peaks characteristic of the spinel structure although according to similar cell parameters ( $8.3919 \text{ \AA}$  and  $8.396 \text{ \AA}$ ; JCPDS card n°22-1086 and 8.396; JCPDS card n°19-062 for  $\text{Fe}_3\text{O}_4$  and  $\text{CoFe}_2\text{O}_4$  respectively),  $\text{Fe}_3\text{O}_4$  and  $\text{CoFe}_2\text{O}_4$  could not be discriminated. Nevertheless, EDX analysis shows atomic Co fraction of 15% for CS-9 and 19% for CS-14, respectively which agree with the presence of a  $\text{CoFe}_2\text{O}_4$  shell of about 1 nm and 1.5 nm thick, respectively.

Cross-sectional images of catalytic layers of the CS-9 NPs drop-casted on a silicon wafer are presented in Fig. 2. One may see that variation of the catalyst loading from  $0.63$  to  $63 \mu\text{g.cm}^{-2}$  results in an increase of the layer thickness from  $\sim 10 \text{ nm}$  (corresponding to 1–2 layers of the NPs) to  $\sim 200 \text{ nm}$ . Irregularities in the layer thickness may be attributed to the deposition method (drop-casting) and the fast evaporation of chloroform, the latter used as a solvent for suspending the NPs.

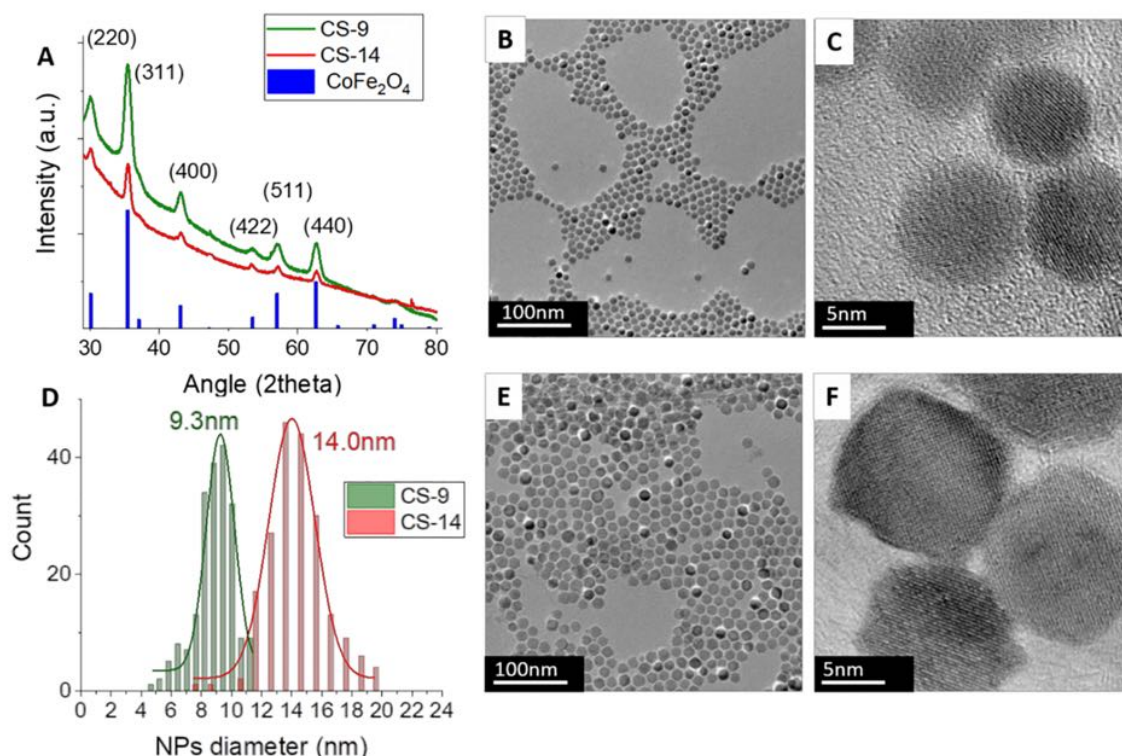
#### 3.2. Electrochemical data

Fig. 3A and D present CVs for CS-9 and CS-14 NPs at different loadings. On both types of NPs, the diminution of the loading results in a diminution of the measured current. Tafel plots constructed from the anodic part of the CV are shown in Fig. 3B and E. The Tafel slopes (Table 1) are in agreement with the results obtained for similar compounds in the literature [2]. In agreement with Chung et al. [9], an increase of the loading leads to an increase of the Tafel slope that can be caused by the ohmic drop built across the catalyst film. Thus, when the loading increases, some zones of the catalytic layer become less involved in the OER as they are not fully submitted to the applied potential. Moreover, increase of the loading results in non-linear Tafel plots with the Tafel slope increasing with the overpotential.

Although the current increases with increasing the catalyst loading, this increase is not directly proportional to it. The mass-weighted activity calculated by dividing the current at 1.67 V vs. RHE by the mass of deposited NPs is constant up to a loading of about  $5 \mu\text{g.cm}^{-2}$  but decreases at higher loadings (Fig. 3F). In an ideal case, if all of the NPs within the catalyst layer are involved in the reaction, the mass-weighted activity should be loading-independent. Here it is not the case, so in agreement with the Tafel plots, these results are suggesting that the NPs are not fully involved in the reaction when the loading is too high.

At high current density, the diminution of the activity with the loading could be due to the formation of oxygen bubbles blocking access of water to the surface sites. To rule out the possible influence of the  $\text{O}_2$  generation, we compared the activity vs. loading plots for two different potentials, 1.62 V (Fig. S1) and 1.67 V (Fig. 3F). By seeing the same trend for both potentials, we infer that the observed loss of activity at high loadings is not related to the formation of  $\text{O}_2$  bubbles. It is also instructive to analyze the activity vs. loading plot shown in Fig. 3F on logarithmic scale. The slope of this plot for high loadings can give an indication of the NPs involvement in the OER. Indeed, a slope of  $-1$  would mean that an increase of the loading does not lead to an increase in the measured OER current. For both CS-9 and CS-14 samples the slope was estimated as  $-0.91$  at 1.67 V vs RHE and decreased down to  $-0.81$  at 1.62 V vs RHE. These values demonstrate that the NPs are becoming less and less involved in the OER reaction while the loading increases, and that this phenomenon aggravates with the increase of the electrode





**Fig. 1.** (A) Diffractograms and (B, E) TEM micrographs of CS-9 (B) and CS-14 (E) NPs, (C, F) HR-TEM micrograph of CS-9 (C) and CS-14 (F). (D) Particle size distributions of CS-9 and CS-14 NPs.

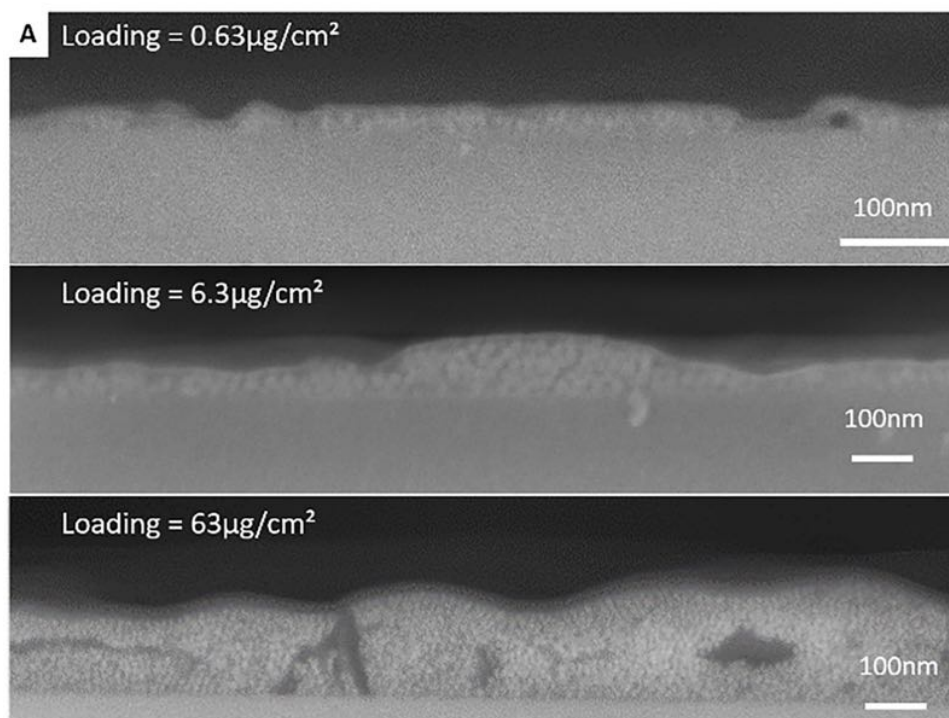


**Fig. 2.** SEM image of a cross section of different loadings of CS-9 NPs drop-casted on a silicon wafer substrate.

potential.

In order to investigate the electrical properties of the catalytic layer, the electrochemical impedance spectroscopy measurements were performed for both types of NP at various loadings. The Nyquist plots presented in Figs. 5 and 6 show that increase of the loading leads to an

increasing asymmetry at high frequencies. The latter could be linked to an additional resistance in the catalytic layer that could either be of an electronic or ionic nature.

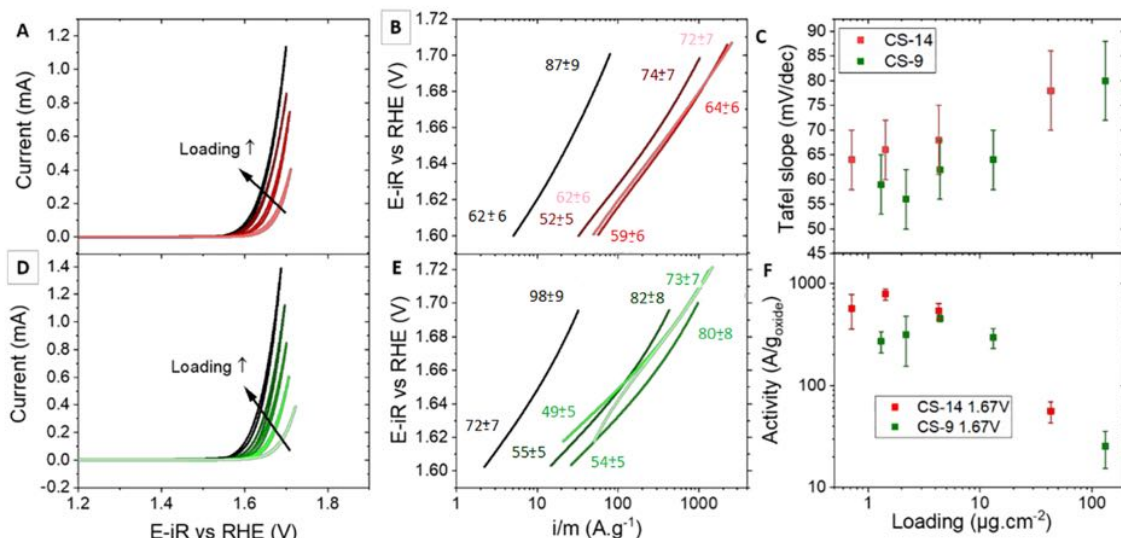


**Fig. 3.** (A, D) CVs and (B, E) corresponding Tafel plots for CS-14 (A, B) and CS-9 NPs (D, E) in 0.1 M NaOH at 10 mV s<sup>-1</sup> scan rate and different catalyst loadings. Dark colors are for high loadings and light ones for lower loadings. (C, F) Evolution of the Tafel slope and mass-weighted activity at 1.67 V vs RHE for CS-9 (green) and CS-14 (red).

**Table 1**

Experimental Tafel slopes determined at 1.62 and 1.67 V vs. RHE as a function of the loading for CS-9 and CS-14 NPs.

Sample	Loading (μg. cm <sup>-2</sup> )	Tafel slope at 1.62 V (mV decade <sup>-1</sup> )	Tafel slope at 1.67 V (mV decade <sup>-1</sup> )
CS-9	131	72 ± 7	98 ± 9
	13.1	55 ± 5	82 ± 8
	4.4	54 ± 5	80 ± 8
	2.2	49 ± 5	73 ± 7
	1.3	60 ± 6	75 ± 7
CS-14	42.8	62 ± 6	87 ± 9
	4.3	52 ± 5	74 ± 7
	1.4	62 ± 6	72 ± 7
	0.7	59 ± 6	64 ± 6

### 3.2. Modelling of the impedance data

In this work, two different models will be considered to fit the impedance data: a simplified Randles circuit without Warburg element and the transmission line model. As the Randles circuit (Fig. 4A) applies to flat electrodes, it is well adapted when the catalyst layer deposited on the electrode is very conductive and all the particles constituting the layer are available for the reaction. Within this model the catalytic layer is considered as homogeneous, in which the ohmic resistance ( $R_s$ , usually related to the electrolyte resistance) and the charge-transfer resistance ( $R_2$ ) do not vary across the film thickness.

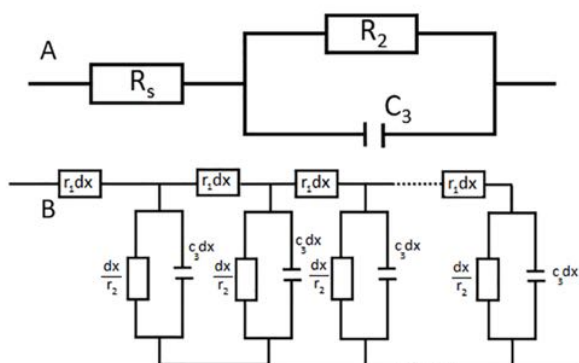


**Fig. 4.** Simplified Randles model (A) and transmission line model (B).

However, when the catalyst layer becomes thicker and/or when the catalytic material is not sufficiently conductive to assure fast charge transport across the layer, one can consider a distributed repartition of the charge transfer at the catalyst/electrolyte interface and electrochemical capacitance within the layer thickness. The catalyst can then be divided into several layers and the modelling can be done using a transmission line model [21] (Fig. 4B). This model considers three different parameters: an apparent resistance  $R_1$ , which may comprise of either the ionic or the electronic resistance or both,  $R_2$  the charge transfer resistance, and  $C_3$  the capacitance. It has been developed for porous polymer and electrocatalyst layers and can thus be applied to porous catalyst films that present a certain resistivity (either ionic or electronic). The equations used to fit the impedance data for the simplified Randles model (1) and the transmission line model (2) are as follows:

$$Z_{\text{Randles}} = \frac{R_2}{1 + jR_2C_3\omega} + R_s \quad (1)$$

$$Z_{\text{Transmission line}} = \left[ \frac{R_1R_2}{1 + \left(j\frac{\omega}{\omega_2}\right)} \right]^{1/2} \times \coth \left( \left( \frac{\omega_2}{\omega_L} \right)^{1/2} \left[ 1 + \left( j\frac{\omega}{\omega_2} \right) \right]^{1/2} \right) \quad (2)$$

The fitting was performed considering pure capacitance, that is a constant phase element with  $\alpha = 1$ . First, the Nyquist plots were fitted at low loadings ( $\sim 1 \mu\text{g.cm}^{-2}$ ) for which the Randles model was proven to be applicable. This allowed the determination of  $R_2$  (the total charge transfer resistance) and  $C_3$  (the capacitance of about a monolayer of NPs). Then, it was possible to fit the Nyquist plots obtained for higher loadings, for which the Randles model was not appropriate, with the transmission line model. The values of the different parameters used in the impedance calculations are given below. Eqs. (3) to (7) were used to calculate the different parameters of the impedance measurement with the transmission line model:  $\omega_2$  (3),  $\omega_L$  (4),  $R_1$  the ionic and electronic resistance in the catalyst layer (5),  $R_2$  the charge transfer resistance of the catalyst layer (6) and  $C_3$  the capacitance (7).  $L$  is the thickness of the layer.

$$\omega_2 = \frac{1}{r_2C_3} = \frac{1}{R_2C_3} \quad (3)$$



$$\omega_L = \frac{1}{r_1 c_3 L^2} = \frac{1}{R_1 C_3} \quad (4)$$

$$R_1 = r_1 \times L \quad (5)$$

$$R_2 = \frac{r_2}{L} \quad (6)$$

$$C_3 = c_3 \times L \quad (7)$$

With the transmission line model there were often several solutions possible for the various parameters of the fit using the method of the least squares. In order to select the right solution, we used the value  $R_2 = r_2/L$  as an initial guess for the nonlinear least squares fitting process.  $r_2$  was estimated thanks to the fitting of the impedance data at low electrocatalyst loading using the Randles model. Thus, among the different possible solutions for the transmission line model, the one presenting the closest  $R_2$  value to the one estimated from Eq. (6) as initial conditions was then selected. The capacitance of the catalytic layer  $C_3$  can also be determined thanks to this model. Fig. 5 presents Nyquist plots for CS-9 and CS-14 fitted with the Randles model for low loadings and the transmission line model for high loadings.

These results evidence that for low loadings (about one or two NP monolayers), the Randles model fits the experimental results. However, when the loading increases, the Randles model does not fit the experimental results anymore and one has to adopt the transmission line model that will consider the electronic and ionic resistance between the catalyst layers (Fig. 6).

From these fittings it was possible to extract the value of  $R_1$ , the resistance (ionic and/or electronic) to the charge transport across the layer, of the charge transfer resistance ( $R_2$ ) and the capacitance of the layer ( $C_3$ ). All these parameters are given in Table 2.

The results shown in Table 2 are demonstrating an influence of the layer thickness for loadings above  $5 \mu\text{g}\cdot\text{cm}^{-2}$  (which corresponds to 10–20 NP monolayers). As expected the value of  $R_2$  decreases with the loading while  $R_1$  and  $C_3$  increase, since a greater number of NPs leads to a higher overall rate of charge transfer across the interface (and hence

the OER current) and higher capacitance. Interestingly, the resistance to the charge transport across the layer ( $R_1$ ) is higher for CS-14 compared to the CS-9 sample for similar loading. This is the reason why the EIS data of the CS-14 sample at  $4.4 \mu\text{g}\cdot\text{cm}^{-2}$  are fitted with the transmission line model, while the Randles model could be used for modeling the EIS data of the CS-9 sample. The higher resistance in the layer comprised of CS-14 nanoparticles might be attributed to their higher amount of Co and thus larger thickness of the non-conductive  $\text{CoFe}_2\text{O}_4$  shell.

Fig. 7 shows the evolution of  $R_2$  and  $C_3$  as a function of the electrode roughness factor defined here as the total surface of NPs (calculated from their mean size determined through TEM measurements) and the geometric surface on the GC electrode ( $\text{cm}^2_{\text{NPs}}\cdot\text{cm}^{-2}_{\text{electrode}}$ ). From these graphs it can be observed that for larger NPs (CS-14), the charge transfer resistance  $R_2$  is lower than the one measured for small particles (CS-9). This difference can be attributed to the larger fraction of Co in the CS-14 nanoparticles, which is involved in the OER active sites.

### 3.3. Simulations of linear sweep voltammograms

The EIS study revealed significant values of  $R_1$ , the resistance to the charge transport across the layer for high catalyst loadings. Using various  $R_1$  values it is also possible to model the linear sweep voltammograms and their respective Tafel slopes for various  $R_1$  values Fig. 8). In order to perform these simulations, the Telegrapher's equations [22] adapted for this model (Eqs. (8)–(10)) were used. Note that the charge-transfer step is modelled as an exponent (see Eq. (9)) with the transfer coefficient of 1 (in agreement with the 60 mV/decade Tafel slope for thin NP films).

$$\frac{\partial V}{\partial x} = -R_1 \times I \quad (8)$$

$$\frac{\partial I}{\partial x} = -V \times ke^{\frac{FV}{RT}} + j\omega C_3 - C_3 \frac{\partial V}{\partial t} \quad (9)$$

$$\frac{\partial V}{\partial t} = v \quad (10)$$

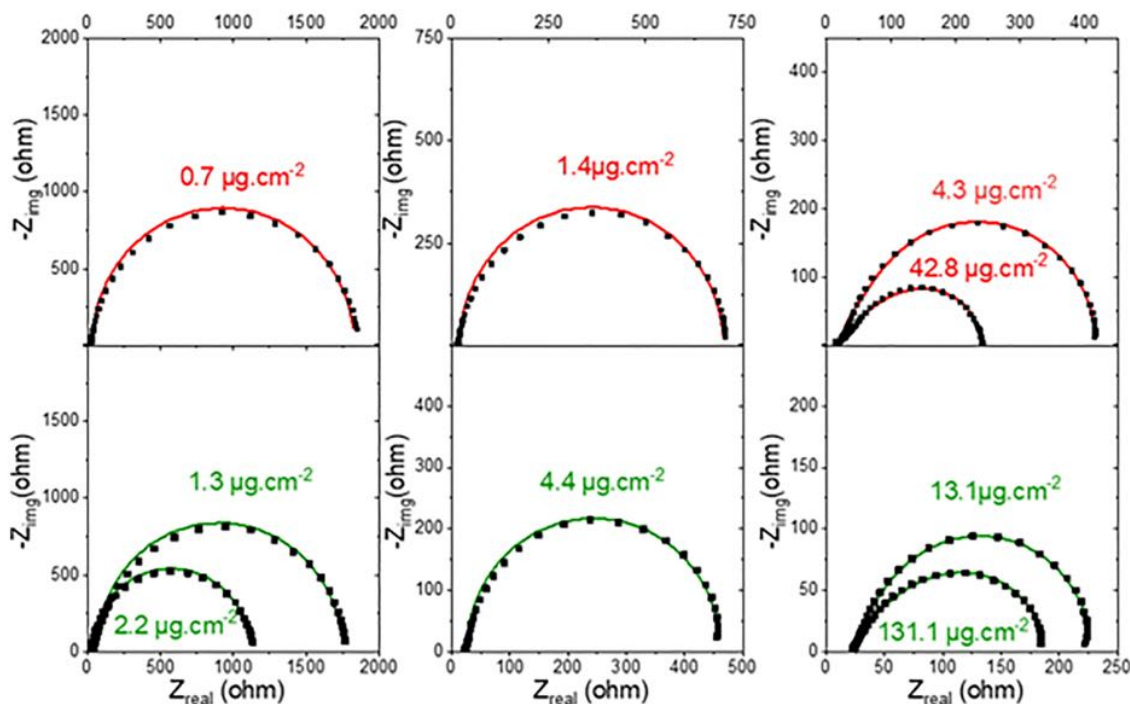
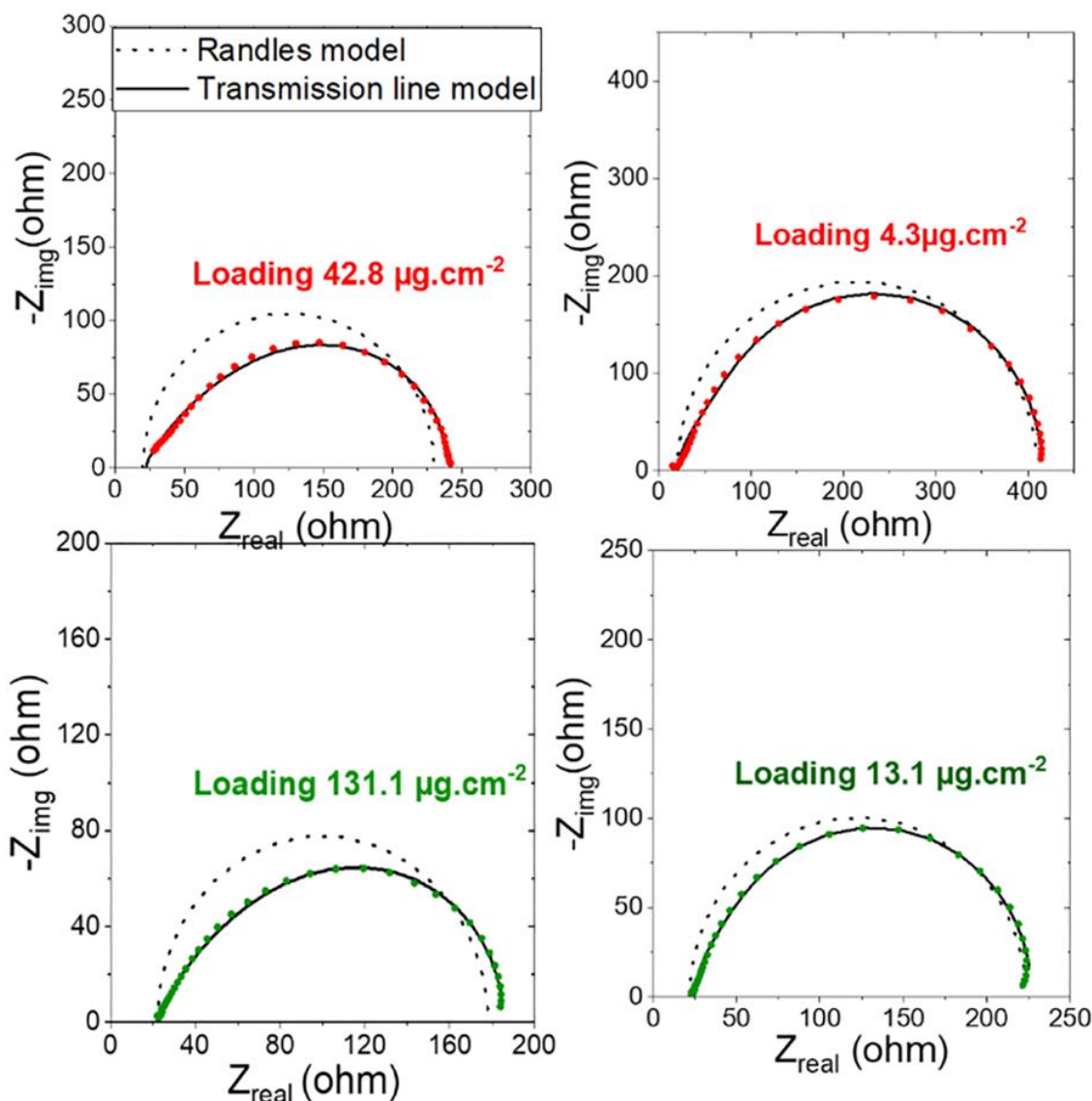


Fig. 5. Experimental (black squares) and computed (solid lines) Nyquist plots for different loadings of NPs on the electrode modelled thanks to the simplified Randles model for low loadings (left and middle) and the transmission line model (right) for high loadings on CS-14 (red) and CS-9 (green) NPs at 1.62 V vs RHE. The GC electrode has a geometric surface of  $0.196 \text{ cm}^2$ .



**Fig. 6.** Transmission line model (solid line) and Randles model (dotted line) fitting of the experimental data (green and red dots) for high loadings of CS-9 (green) and CS-14 (red) NPs. The surface area of the GC electrode is 0.196 cm<sup>2</sup>.

**Table 2**

$R_2$ ,  $R_1$ , and  $C_3$  parameters obtained thanks to the fitting of the EIS spectra. The geometric surface area of the GC electrode is 0.196 cm<sup>2</sup>.

Sample	Loading (µg.cm <sup>-2</sup> )	$R_2$ (ohm)	$R_1$ (ohm)	$C_3$ (µF)
CS-9	131.1	20±5	1317±330	2790±700
	13.1	144±36	191±50	142±40
	4.4	437±110	/	118±30
	2.2	1090±270	/	46±11
	1.3	1690±420	/	22±5
CS-14	42.8	30±8	1575±400	870±220
	4.3	304±75	293±75	72±20
	1.4	679±170	/	46±11
	0.7	1800±450	/	28±7

Eqs. (8)–(10) are the Telegraphers equations.  $V$  is the applied voltage,  $C = 10^{-5}$  F the capacitance,  $I$  the current,  $k = 10^{-5}$  S, the conductance associated to the reaction rate constant,  $T = 298$  K the temperature,  $R = 8.314$  J.K<sup>-1</sup> mol<sup>-1</sup> the ideal gas constant and  $F = 96,485$  C. mol<sup>-1</sup> the Faraday constant.

These simulated linear sweep voltammetry curves exhibit a decrease in the current when the  $R_1$  value increases (Fig. 8A). Also, the Tafel plots

deviate from an ideal linear behavior and are becoming convex when the  $R_1$  increases (Fig. 8B). These observations agree with the experimental data presented above. These results confirm that the catalytic activity cannot be determined accurately for high loadings if the catalyst layer presents resistance to charge transport across the layer. This resistance may arise from an insufficient electronic conductivity of the catalytic layer (poorly conducting catalyst particles or high contact resistance between the catalytic particles) or, alternatively, from ionic resistance of the electrolyte within the pores of the catalytic layer. Also, this highlights the impact of the loading on the Tafel slope, the latter being often used for mechanistic interpretations. Indeed, these interpretations are likely to be inaccurate for high loadings, notably for poorly conductive catalysts and/or electrolytes of low conductivity.

The simulated currents normalized by the layer thickness in the transmission line model were then plotted against the transmission line length ( $L$ ) for two different potentials (0.12 and 0.17 V) (Fig. 9). We note that as the thickness increases (and thus the resistance across the layer,  $R_1$ , increases), the normalized current drops and the slope of the log  $I$  vs log  $L$  changes with the applied potential from -0.68 at 0.12 V to -0.9 at 0.17 V. The overall trend and the simulated values are in reasonable agreement with the experimental data presented above.



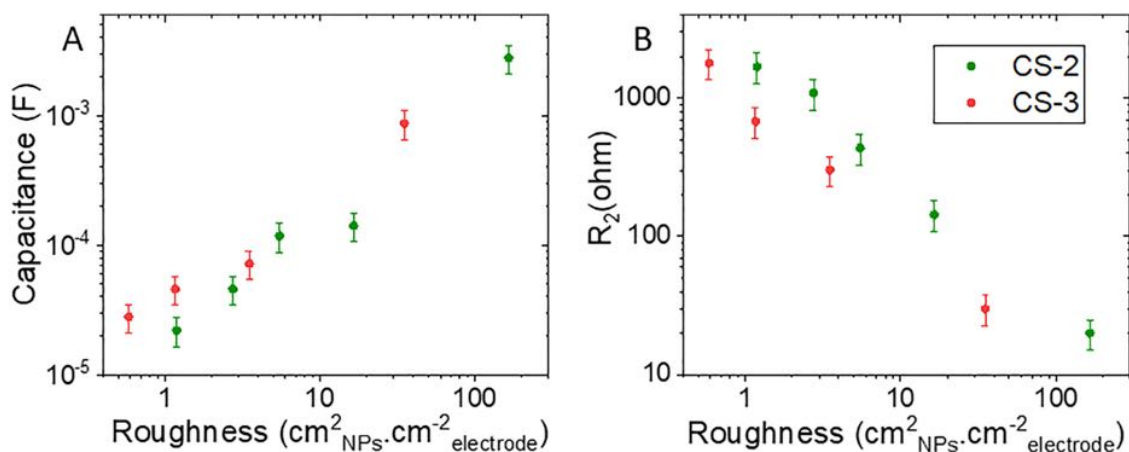


Fig. 7. Evolution of the capacitance  $C_3$  (A) and the charge transfer resistance  $R_2$  (B) as a function of the roughness of the catalytic layer defined as the total surface of NPs (calculated from their mean size) and the geometric surface on the GC electrode ( $\text{cm}^2_{\text{NPs}} \cdot \text{cm}^{-2}_{\text{electrode}}$ ). The geometric surface area of the GC electrode is  $0.196 \text{ cm}^2$ .

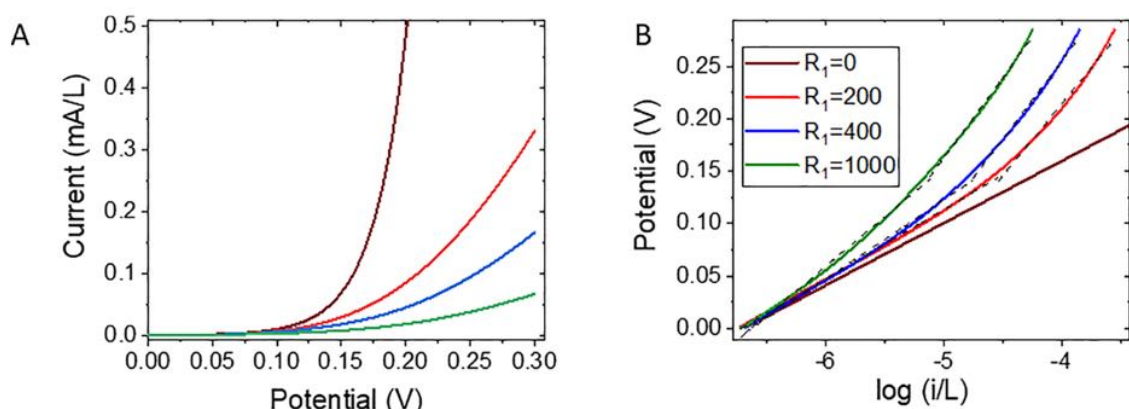


Fig. 8. Simulated linear sweep voltammetry curves (A) and their corresponding Tafel plots (B).

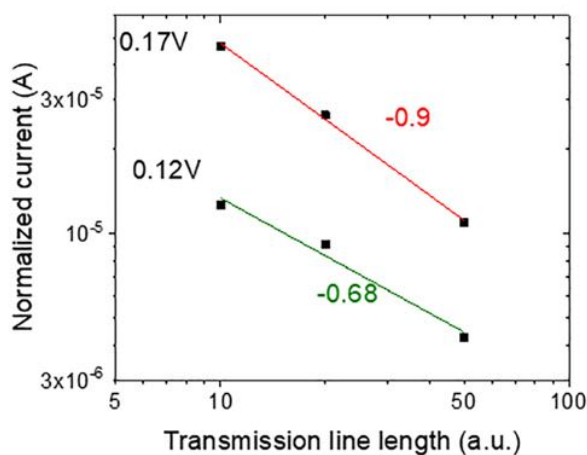


Fig. 9. Simulated currents normalized by the number of elements at 0.12 and 0.17 V against the transmission line length in the transmission line model.

Finally, in Fig. 10 the current and the potential distribution inside the catalytic layer have been plotted for a high value of  $R_1 = 1000 \Omega$  and for different values of the high applied potential from 0 to 0.3 V. The influence of other values of  $R_1$  on the potential distribution is displayed in Fig. S2.

Fig. 10 demonstrates that when the potential is increased above 0.1 V, it is applied in a very inhomogeneous manner within the catalyst

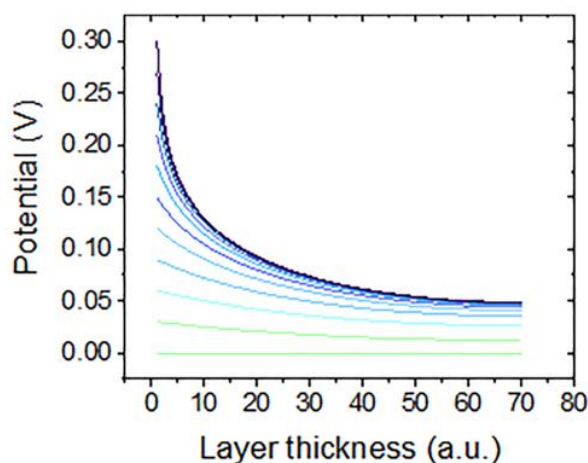


Fig. 10. Simulation of the potential distribution within the catalyst layer for various potentials applied on the working electrode and a  $R_1$  resistance of  $1000 \Omega$ .

layer. If the apparent  $R_1$  resistance is primarily electronic, then the highest potential is applied to the catalyst particles adjacent to the substrate (GC in the experiment) decaying towards the exterior of the catalyst layer. On the contrary, if the apparent  $R_1$  resistance is primarily ionic, then the highest potential is applied to the exterior of the catalyst layer, facing the electrolyte, decaying towards the interior of the catalyst



layer. As a result, the current generated due to the electrocatalytic reaction will be the highest in the interior of the catalyst layer (electronic resistance) or in the exterior of the catalyst layer (ionic resistance). This confirms that at high loadings the NPs are not entirely involved in the electrode reaction.

#### 4. Conclusion

To conclude, in this work we studied the OER activity of two different sizes of core-shell cobalt iron oxide NPs at different thickness of the catalytic layer. For both types of NPs, it was observed that the apparent activity of the NPs at a given potential strongly depends on the layer's thickness and that the Tafel plots deviate from linear and increase with the loading from 60 to 80 mV/decade. It was concluded that in order to measure accurately the activity of a catalyst, thin layers must be used, notably for catalyst layers that are not highly conductive. The activity decay can be attributed to either contact resistance between the NPs or to the electrolyte resistance in the voids between the NPs. In order to distinguish between these two alternatives, additional experiments are required, notably with variable electrolyte conductivity.

In order to get a better understanding of the influence of the resistance across the catalyst layer on the measured electrochemical characteristics (mass-weighted activity and Tafel slope), impedance spectroscopy measurements were performed. These measurements revealed asymmetry of the Nyquist plots at high frequencies for high loadings. Consequently, we used the transmission line model to extract the apparent resistance (ionic and/or electronic) value from the fitting of these impedance data and used the resistance value to simulate the linear sweep voltammetry curves for various  $R_1$  values. These simulations agreed with the experimental data as for higher resistance the normalized current was lower and the Tafel plots were deviating from an ideal linear behavior, confirming that mechanistic interpretations of the Tafel slopes are only accurate if the catalyst is highly conductive (negligible resistance to the charge transport across the catalyst layer) or if the loading on the electrode is low. Finally, the potential distribution throughout the catalytic layer was also simulated and displayed an exponential decay when the resistance was important, confirming that the particles within the layer were not submitted to the same potential and consequently that if the catalytic layer is too thick not all the particles will be equally involved in the electrocatalytic reaction.

#### CRedit authorship contribution statement

**Lisa Royer:** Conceptualization, Methodology, Investigation, Data curation, Writing – original draft. **Julie Guehl:** Investigation. **Maud Zilbermann:** Investigation. **Thierry Dintzer:** Resources. **Cédric Leuvey:** Resources. **Benoit P. Pichon:** Supervision, Writing – review & editing. **Elena Savinova:** Supervision, Writing – review & editing. **Antoine Bonnefont:** Supervision, Writing – review & editing.

#### Declaration of Competing Interest

The authors declare that they have no known competing financial interests or personal relationships that could have appeared to influence the work reported in this paper.

#### Data availability

Data will be made available on request.

#### Acknowledgments

Project financially supported by the Foundation for Frontier Research in Chemistry. The authors acknowledge Barbara Freis for the TEM images. The SEM platform (MEB-CRO) as well as the XRD platform

of IPCMS laboratory.

#### Supplementary materials

Supplementary material associated with this article can be found, in the online version, at doi:10.1016/j.electacta.2023.141981.

#### References

- [1] F. Song, L. Bai, A. Moysiadou, S. Lee, C. Hu, L. Liardet, X. Hu, Transition metal oxides as electrocatalysts for the oxygen evolution reaction in alkaline solutions: an application-inspired renaissance, *J. Am. Chem. Soc.* 140 (25) (2018) 7748–7759, <https://doi.org/10.1021/jacs.8b04546>.
- [2] J. Peng, W. Dong, Z. Wang, Y. Meng, W. Liu, P. Song, Z. Liu, Recent advances in 2D transition metal compounds for electrocatalytic full water splitting in neutral media, *Mater. Today Adv.* 8 (2020), 100081, <https://doi.org/10.1016/j.mtdadv.2020.100081>.
- [3] W. Baaziz, B.P. Pichon, S. Fleutot, Y. Liu, C. Lefevre, J.-M. Grenèche, M. Toumi, T. Mhiri, S. Begin-Colin, Magnetic iron oxide nanoparticles: reproducible tuning of the size and nanosized-dependent composition, defects, and spin canting, *J. Phys. Chem. C* 118 (7) (2014) 3795–3810, <https://doi.org/10.1021/jp411481p>.
- [4] W. Baaziz, B.P. Pichon, Y. Liu, J.-M. Grenèche, C. Ulhaq-Bouillet, E. Terrier, N. Bergeard, V. Halté, C. Boeglin, F. Choueikani, M. Toumi, T. Mhiri, S. Begin-Colin, Tuning of synthesis conditions by thermal decomposition toward core-shell  $\text{CoFe}_2\text{O}_4$  nanoparticles with spherical and cubic shapes, *Chem. Mater.* 26 (17) (2014) 5063–5073, <https://doi.org/10.1021/cm502269s>.
- [5] W. Wang, J. Luo, S. Chen, Carbon oxidation reactions could misguide the evaluation of carbon black-based oxygen-evolution electrocatalysts, *Chem. Commun.* 53 (84) (2017) 11556–11559, <https://doi.org/10.1039/C7CC04611A>.
- [6] F.N. Skomurski, S. Kerisit, K.M. Structure Rosso, Charge distribution, and electron hopping dynamics in magnetite ( $\text{Fe}_3\text{O}_4$ ) (100) Surfaces from First Principles, *Geochim. Cosmochim. Acta* 74 (15) (2010) 4234–4248, <https://doi.org/10.1016/j.gca.2010.04.063>.
- [7] M. Pauly, J.F. Dayen, D. Golubev, J.B. Beaufrand, B.P. Pichon, B. Doudin, S. Begin-Colin, Co-tunneling enhancement of the electrical response of nanoparticle networks, *Small* 8 (1) (2012) 108–115, <https://doi.org/10.1002/smll.201100931>.
- [8] G. Rydzek, D. Toulemon, A. Garofalo, C. Leuvey, J.-F. Dayen, D. Felder-Flesch, P. Schaaf, L. Jierry, S. Begin-Colin, B.P. Pichon, F. Boulmedais, Selective nanotrench filling by one-pot electroclick self-constructed nanoparticle films, *Small* 11 (36) (2015) 4638–4642, <https://doi.org/10.1002/smll.201500639>.
- [9] D.Y. Chung, S. Park, P.P. Lopes, V.R. Stamenkovic, Y.-E. Sung, N.M. Markovic, D. Strmcnik, Electrokinetic analysis of poorly conductive electrocatalytic materials, *ACS Catal.* 10 (9) (2020) 4990–4996, <https://doi.org/10.1021/acscatal.0c00960>.
- [10] G. Chen, C.C. Waraksa, H. Cho, D.D. Macdonald, T.E. Mallouk, EIS studies of porous oxygen electrodes with discrete particles: I. impedance of oxide catalyst supports, *J. Electrochem. Soc.* 150 (9) (2003) E423, <https://doi.org/10.1149/1.1594729>.
- [11] H.K. Song, Y.H. Jung, K.H. Lee, L.H. Dao, Electrochemical impedance spectroscopy of porous electrodes: the effect of pore size distribution, *Electrochim. Acta* 44 (20) (1999) 3513–3519, [https://doi.org/10.1016/S0013-4686\(99\)00121-8](https://doi.org/10.1016/S0013-4686(99)00121-8).
- [12] C. Heim, N. Wagner, K.A. Friedrich, Analytical distribution function of relaxation times for porous electrodes and analysis of the distributions of time constants, *Solid State Ion.* 383 (2022), 115960, <https://doi.org/10.1016/j.ssi.2022.115960>.
- [13] C.C. Waraksa, G. Chen, D.D. Macdonald, T.E. Mallouk, EIS studies of porous oxygen electrodes with discrete particles: II. transmission line modelling, *J. Electrochem. Soc.* 150 (9) (2003) E429, <https://doi.org/10.1149/1.1594730>.
- [14] A. Papaderakis, D. Tsiplakides, S. Balomenou, S. Sotiriopoulos, Electrochemical impedance studies of  $\text{IrO}_2$  catalysts for oxygen evolution, *J. Electroanal. Chem.* 757 (2015) 216–224, <https://doi.org/10.1016/j.jelechem.2015.09.033>.
- [15] K. Sartori, A. Musat, F. Choueikani, J.-M. Grenèche, S. Hettler, P. Bencok, S. Begin-Colin, P. Steadman, R. Arenal, B.P. Pichon, A detailed investigation of the onion structure of exchanged coupled magnetic  $\text{Fe}_3\text{-}\delta\text{O}_4/\text{CoFe}_2\text{O}_4/\text{Fe}_3\text{-}\delta\text{O}_4$  nanoparticles, *ACS Appl. Mater. Interfaces* 13 (14) (2021) 16784–16800, <https://doi.org/10.1021/acsami.0c18310>.
- [16] X. Liu, B.P. Pichon, C. Ulhaq, C. Lefevre, J.M. Grenèche, D. Bégin, S. Bégin-Colin, Systematic study of exchange coupling in core-shell  $\text{Fe}_3\text{-}\delta\text{O}_4/\text{CoO}$  nanoparticles, *Chem. Mater.* 27 (11) (2015) 4073–4081, <https://doi.org/10.1021/acs.chemmater.5b01103>.
- [17] The 2020 EU Critical Raw Materials List (2022). <https://www.iea.org/policies/15274-the-2020-eu-critical-raw-materials-list/> (accessed 2022-10-26).
- [18] G. Cotin, C. Kiefer, F. Perton, M. Boero, B. Özdamar, A. Bouzid, G. Ori, C. Massobrio, D. Bégin, B. Pichon, D. Mertz, S. Begin-Colin, Evaluating the critical roles of precursor nature and water content when tailoring magnetic nanoparticles for specific applications, *ACS Appl. Nano Mater.* 1 (8) (2018) 4306–4316, <https://doi.org/10.1021/acsanm.8b01123>.
- [19] F. Perton, Architecture de nanoparticules hybrides pour une imagerie et/ou thérapie multimodales. Doctoral Dissertation, Université de Strasbourg, 2019. <http://www.theses.fr/2019STRAE043> (accessed 2022-03-03).
- [20] L. Royer, A. Bonnefont, T. Asset, B. Rotonelli, J.J. Velasco-Vélez, S. Holdcroft, S. Hettler, R. Arenal, B. Pichon, E. Savinova, Cooperative redox transitions drive electrocatalysis of the oxygen evolution reaction on cobalt-iron core-shell

- nanoparticles, ACS Catal. 13 (1) (2023) 280–286, <https://doi.org/10.1021/acscatal.2c04512>.
- [21] S. Fletcher, An electrical model circuit that reproduces the behaviour of conducting polymer electrodes in electrolyte solutions, J. Electroanal. Chem. 337 (1) (1992) 127–145, [https://doi.org/10.1016/0022-0728\(92\)80533-A](https://doi.org/10.1016/0022-0728(92)80533-A).
- [22] J. Masoliver, G.H. Weiss, Telegrapher's equations with variable propagation speeds, Phys. Rev. E 49 (5) (1994) 3852–3854, <https://doi.org/10.1103/PhysRevE.49.3852>.